Electronic Supplementary Information

Interlayer Electronic Coupling Regulates performance of FeN MXenes and Fe_2B_2 MBenes as High-Performance Li- and Al- ion Batteries.

Jiafei Pang[a], Wenyuan Jin[b], Xiaoyu Kuang[a]* and Cheng Lu[c]*

[a] Institute of Atomic and Molecular Physics, Sichuan University, Chengdu, 610065, China

[b] Institute of Physics, Henan Academy of Sciences, Zhengzhou 450046, PR China

[c] School of Mathematics and Physics, China University of Geosciences (Wuhan), Wuhan, 430074, China

Corresponding author: scu_kuang@163.com lucheng@calypso.cn

The ground state structural search of 2D FeN is carried out using the unbiased Crystal structure AnaLYsis by Particle Swarm Optimization (CALYPSO) structural search method. We focus on the stoichiometry of 1:1, specifically the FeN composition, during the structural searching, which includes 1-4 formula units (f. u.). The initial structures are randomly constructed using planar group symmetry operations and then relaxed. To optimize efficiency, 60% of the lower-enthalpy structures are selected to produce the next generation, while the remaining 40% are randomly constructed using PSO. The structural searching simulations stop after 20 generations. To avoid interactions between adjacent layers due to periodicity, all monolayer structures are separated by a vacuum space of at least 15 Å in the z-direction. For structural optimizations and energy calculations, we employ the Vienna ab initio simulation package (VASP).

Fig. 6(b) shows the schematics of the Al ion theoretical capacity and energy barrier for transition metal carbons and nitrogen compounds, including tetr-VC,[1] Mo_2ScC_2, Mo_2TaC_2,[2] C_2N,[3] $(Mo_{2/3}Sc_{1/3})_2CO_2$,$(Mo_{2/3}Sc_{1/3})_2C$,[4] Fe_2CS_2,[5] WS_2,[6] Ti_2CS_2, GeP_3.[7] B_36 exhibits an energy barrier of 0.039 eV and theoretical capacities of 9917 mA h g^{-1} as AlBs batteries.[8] However, it does not contain metal ions and is not shown in Fig 6(b). The adsorption properties for Aluminum-ion batteries, including the specific capacity, migration barrier, volume change, open circuit voltage, and the electronic band, are summarized in Table S6. The FeN monolayer has namely appropriate pore size, crossed the Fe-N bonds, and entirely planar structure, can help achieve ultrahigh capacity, but the larger adsorption energy effect the Al atom diffuse inducing high energy barrier. The FeN/Fe_2B_2 heterojunction have larger capacity with lower migration barrier, which can encourage further studies of Fe-based 2D materials for Aluminum-ion batteries.

To expand the application of FeN/Fe_2B_2 heterojunction, particularly in electrochemical cells, we consider its potential use in the hydrogen evolution reaction (HER). The HER pathway involves three processes: $H^+ + e^-$ on the supplying the electrons electrode (initial state), adsorbed H^* on the surface (intermediate), and $1/2H_2$ as the product. To evaluate the catalytic performance of the catalyst, we use a 2×2×1 supercell as a substrate and calculate the intermediate Gibbs free energy (ΔG_{H^*}). A negative value for

ΔG_{H^*} indicates better catalytic performance. ΔG_{H^*} is calculate by $\Delta G_{H^*} = \Delta E_H + \Delta E_{ZPE}$ - $T\Delta S_H$, where ΔE_H, ΔE_{ZPE} are the adsorption energy, the zero-point energy, respectively. $T\Delta S_H$ represents the entropy change between the adsorbed and product states at finite temperature T. We then use the concise formula $\Delta G_{H^*} = \Delta E_H + 0.24$ eV, which has been tested in various studies. Our calculations indicate that FeN/Fe_2B_2 heterojunction exhibits a coverage of 1/4H* and a corresponding ΔG_{H^*} of 0.03 eV. This value is slightly lower than that of MoS_2 (0.14 eV) or WS_2 (0.22 eV), suggesting the heterojunction's potential applications for hydrogen evolution.

Monte Carlo calculations are used to determine the most favorable adsorption sites for Al ions. The Al atoms are placed at locations with more than 2.2 Å between two Al atoms and the distances between the Al atoms and the substrate ranging from 5.7 Å to 1.9 Å. The MC simulation provides a large number of structures, the VASP software is used for the structural optimization is carried by three steps. Low-precision structural optimization is calculated the with convergence criteria of 10^{-4} eV for energy and -0.05 eV $Å^{-1}$ for force. The cell volume is allowed to change. The medium accuracy optimization is performed with convergence criteria of 10^{-5} eV for energy and -0.05 eV $Å^{-1}$ for force and the positions of atoms are allowed to change. Then the high accuracy optimization is performed until energy convergence.

Table S1: The structure information including lattice parameters and atomic coordinates of FeN, Fe_2B_2 monolayers, and FeN/Fe_2B_2 heterojunction.

Formula of Unit Cell	Lattice Parameters	Fractional Coordinates of Atoms
FeN	a=2.803 Å	Fe(0.500 0.500 0.500)
	b=2.803 Å	N (0.000 0.000 0.500)
	c=15.000 Å	
Fe_2B_2	a=2.830 Å	Fe1 (0.499 0.499 0.736)
	b=2.800 Å	Fe2 (0.000 0.500 0.519)
	c=19.788 Å	B1 (0.499 0.000 0.569)
		B2 (0.000 0.000 0.685)
FeN/Fe_2B_2	a=2.746 Å	Fe1 (0.500 0.500 0.492)
	b=2.712 Å	Fe2 (0.000 0.500 0.381)
	c=20.161 Å	Fe3 (0.500 0.500 0.610)
		B1 (0.500 0.000 0.406)
		B2 (0.000 0.000 0.462)
		N (0.000 0.000 0.624)

Table S2: Calculated elastic constants of FeN monolayer, FeN/Fe_2B_2 heterojunction and comparison materials. Elastic constants C_{ij} in units of N/m.

Phase	C_{11}	C_{22}	C_{12}	C_{66}
FeN	66	66	45	54
Fe_2B_2 [9]	111	92	33	47
FeN/Fe_2B_2	105	88	71	65
Graphene [10]	358	358	65	147
Borophone [11]	398	170	-7	94
B_2C/Graphene [12,13]	642	533	79	230
WS_2 [13]	130	130	55	37
Graphene/WS_2 [13]	479	479	88	195
α-B_3C_2 [14]	305	305	67	121
B_2C [14]	290	290	146	90
B_4C [14]	340	340	51	144
α-magnesene [15]	36	36	4	16
B_7P_2 [16]	175	173	45	63
Ti_3C_2 [17]	253	48	252	102
Ti_3BN [17]	187	33	190	77
C_3N_5 [18]	373	373	58	156
C_3B [19]	265	50	112	255

Table S3: Structure details and electronic properties of FeN, Fe_2B_2, monolayers, and FeN/Fe_2B_2 heterojunction are presented. Total Magnetic Moment per unit cell (M), Bond Length B_L(Fe-M) of Fe-B(N) (M for B or N atom), Work function (ϕ), Charge Transfer (C_T) for B or N atoms. Positive and negative C_T values represent electron gain and loss, respectively.

Phase	M	B_L(Fe-M)	ϕ	C_T(B1/B2/N)	C_T(Fe1/Fe1/Fe3)
FeN	0	1.98	5.06	1.12	-1.13
Fe_2B_2	0	2.43	4.94	0.50/0.45	-0.47/-0.48
FeN/Fe_2B_2	0	1.92/2.02	5.47	0.28/0.35/1.02	-0.38/-0.32/-0.95

Table S4: Date of Li adsorption on the FeN/Fe_2B_2 heterojunction include the following parameters: Bader charge (B/e), Distance between the Li ion and the substrate (D/Å), Work function (E_{wf}/eV), Area of the substrate surface(S/Å^2), E_{ea}, and E_{coul} respectively. Here, E_{ea} is calculated as the sum of the work function E_{wf} and the charge (B). The Coulomb energy E_{coul} can be approximated by -14.38q^2/2D, where D represents the distance between the Li cation and the substrate.[9]

Phase	B	D	E_{wf}	S	E_{ea}	E_{coul}
FeN	0.87	1.48	3.42	28.69	2.99	3.72
Fe_2B_2	0.83	2.33	3.99	32.44	3.33	2.14
FeN/Fe_2B_2	0.88	1.49	3.79	31.10	3.34	3.71

Table S5: Date of Al adsorption on the FeN/Fe_2B_2 heterojunction include the following parameters: Bader charge (B/e), Distance between the Li ion and the substrate (D/Å), Work function (E_{wf}/eV), Area of the substrate surface(S/Å^2), E_{ea}, and E_{coul}, respectively.

Phase	B	D	E_{wf}	S	E_{ea}	E_{coul}
FeN	0.80	1.84	4.73	26.18	3.79	2.43
Fe_2B_2	0.81	2.28	4.18	32.31	3.42	2.11
FeN/Fe_2B_2	0.81	1.90	5.04	30.92	4.13	2.53

Table S6: Comparison of specific capacity (C/mA h g^{-1}), migration barrier (B/eV), adsorption energies (E_{ad}/eV/Al) at the preferred adsorption sites, mean open circuit voltage (OCV/V), and the electronic band (E/eV) of monolayer and heterojunction for Aluminum-ion batteries. ' - ' means data unavailable.

Phase	C	B	E_{ad}	OCV	E
FeN/Fe_2B_2	4254	0.01	-2.13	0.60	Metallic
B_{36} [8]	9917	0.03	-	1.32	Metallic
FeN	9207	0.86	-5.20	1.08	Metallic
tetr-CrC [1]	1450	0.21	-	0.15	Metallic
tetr-VC [1]	1150	0.10	-	0.13	Metallic
C_2N [3]	1175	3.00	-0.04	0.78	Metallic
Fe_2CO_2 [2]	775	0.71	-5.31	-	-
Fe_2CS_2 [2]	642	0.47	-0.09	-	Metallic
Ti_2CO_2 [2]	288	0.76	-	-	0.64
$(Mo_{2/3}Sc_{1/3})_2C$ [4]	886	0.57	-	0.75	Metallic
$(Mo_{2/3}Sc_{1/3})_2CO_2$ [4]	630	0.63	-4.95	0.80	0.58
GeP_3 [7]	182	0.64	-0.23	-0.09	Metallic
g-Mg_3N_2 [2]	797	0.93	-3.71	0.01	0.91
Mo_2TaC_2 [5]	888	0.11	-0.80	0.40	Metallic
Mo_2ScC_2 [5]	1170	0.15	-1.02	0.20	Metallic
WS_2 [6]	531	0.25	-1.39	3.31	1.79

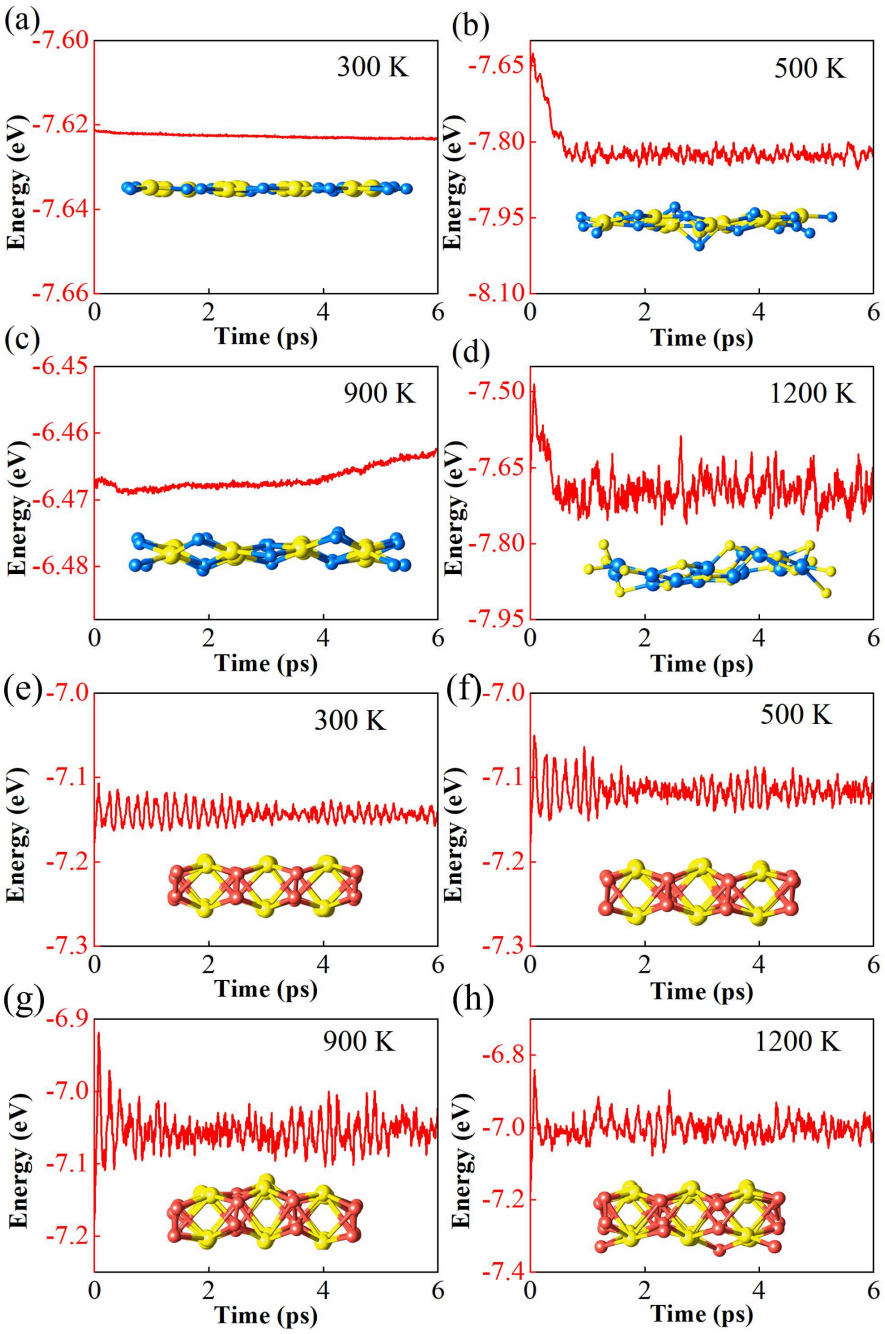

Figure S1: The free energies per atom and the last snapshots of FeN monolayer are obtained after simulating AIMD at (a) 300 K, (b) 500 K, (c) 900 K, and (d) 1200 K for 6 ps. In the snapshots, Fe and N atoms are represented by yellow and blue balls, respectively. The free energies per atom and the last snapshots of Fe_2B_2 are obtained after simulating AIMD at (e) 300 K, (f) 500 K, (g) 900 K, and (h) 1200 K for 6 ps. In the snapshots, Fe and B atoms are represented by yellow and orange balls, respectively.

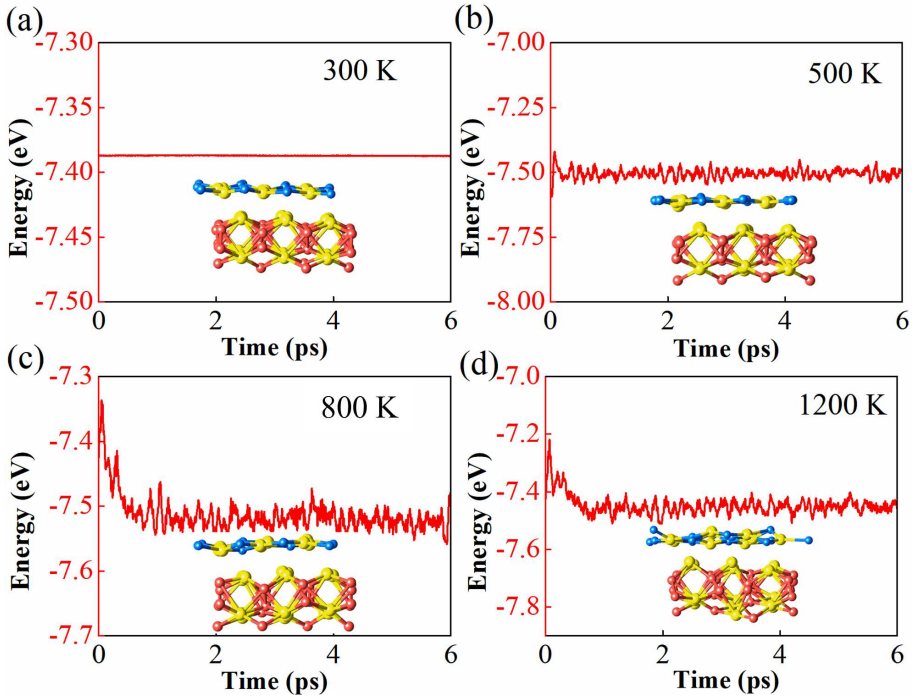

Figure S2: The free energies per atom and the last snapshots of the FeN/Fe_2B_2 heterojunction by simulating AIMD at 300 K, 500 K, 800 K, and 1200 K for 6 ps, Fe, B, and N atoms are represented by yellow, orange, and blue balls, respectively.

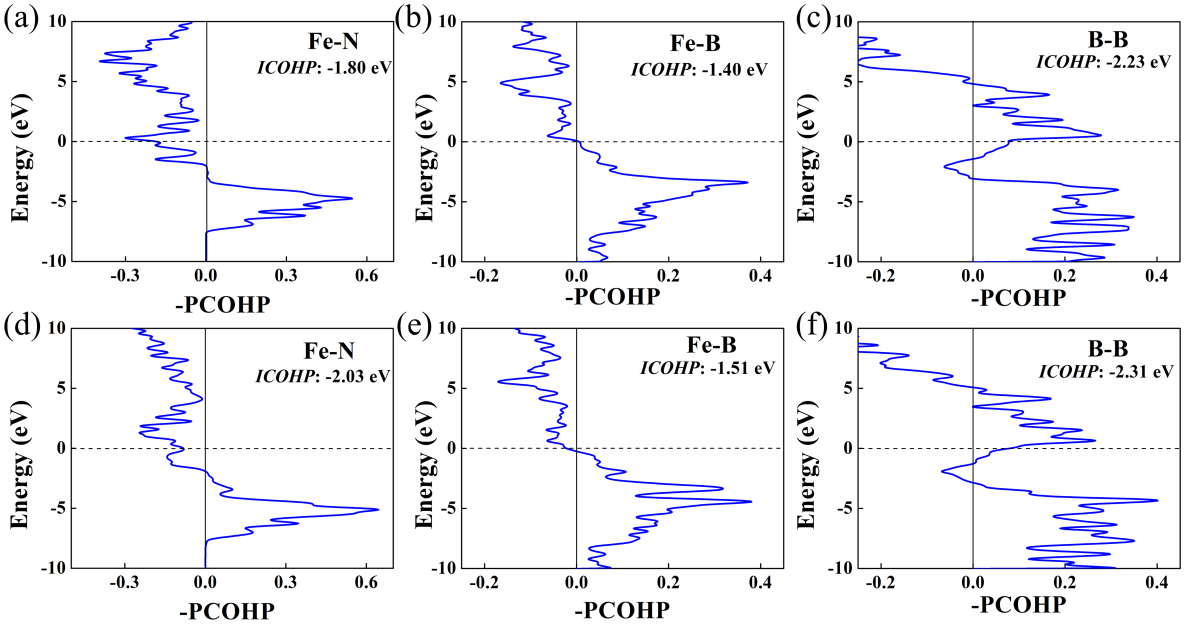

Figure S3: The calculated crystal orbital Hamilton population (COHP) analysis is performed for (a) Fe-N, (b) Fe-B, and (c) B-B bonding interactions in the FeN monolayer and Fe_2B_2 monolayer. Additionally, the COHP analysis is conducted for (d) Fe-N, (e) Fe-B, and (f) B-B bonds in the FeN/Fe_2B_2 heterojunction. The ICOHP values (in eV/bond) are listed for comparison.

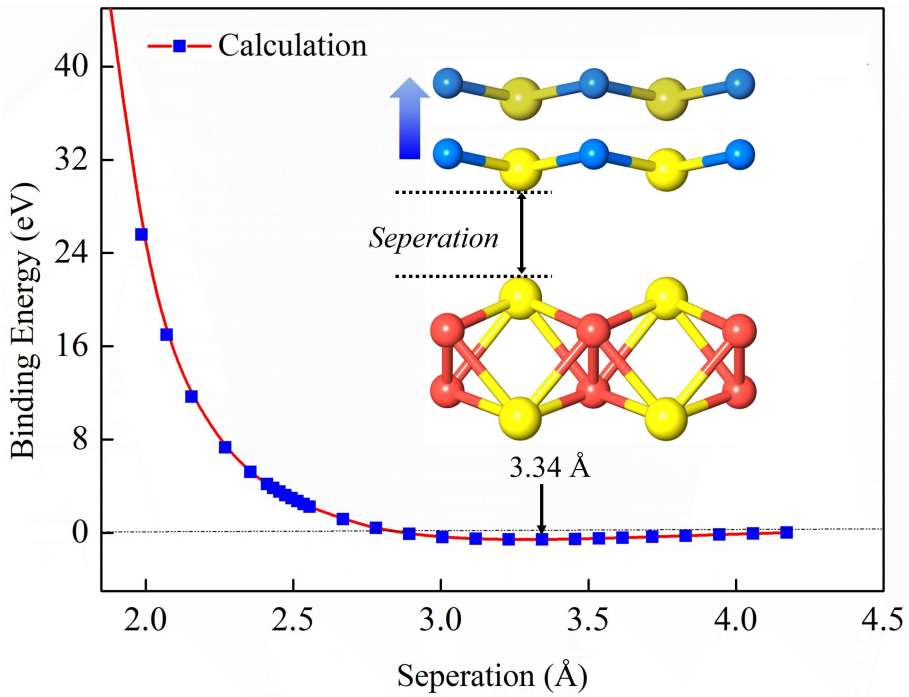

Figure S4: The Binding energy values of the FeN/Fe_2B_2 heterojunction at different separation distances.

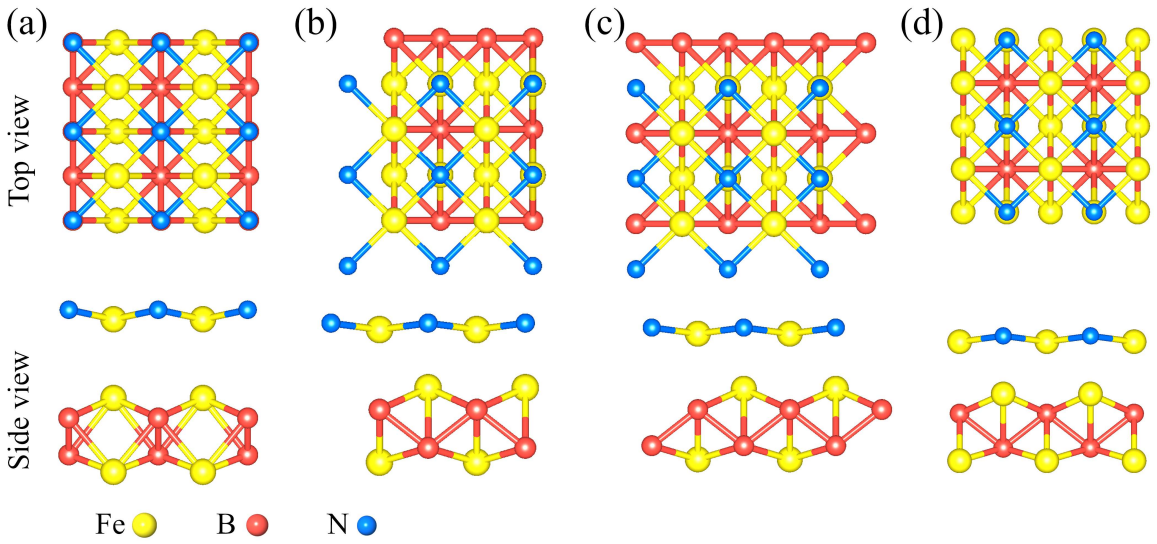

Figure S5: (a-d) Top and side views for different stacking configurations of the FeN/Fe_2B_2 heterojunctions.

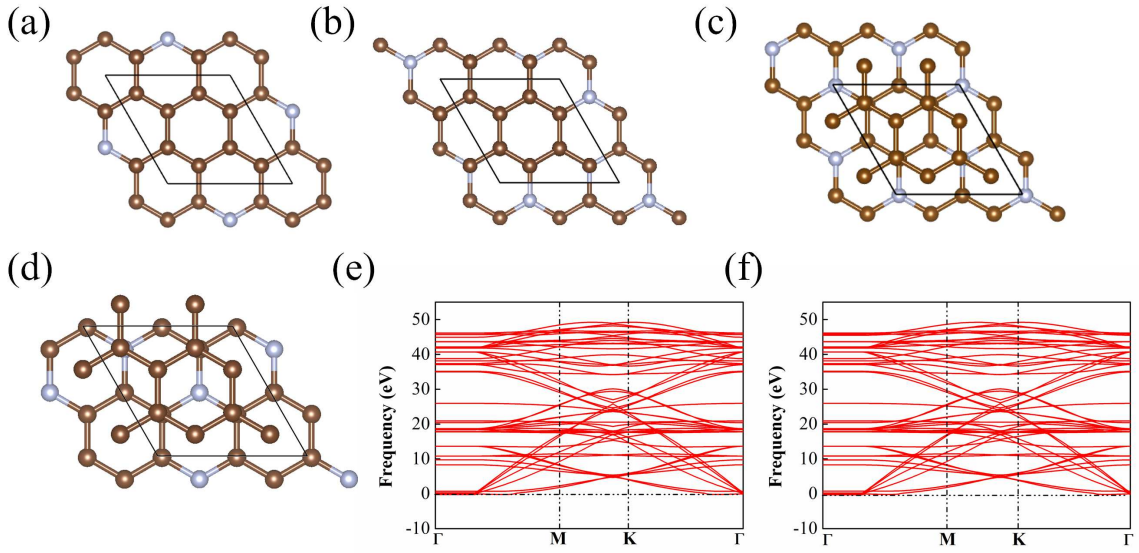

Figure S6: (a-d) Top side views for different C_3N/Graphene heterojunction configurations. (e) Calculated phonon dispersion curves for the structure c. (f) Calculated phonon dispersion curves for the structure d. The dark and light balls represent C and N atoms, respectively.

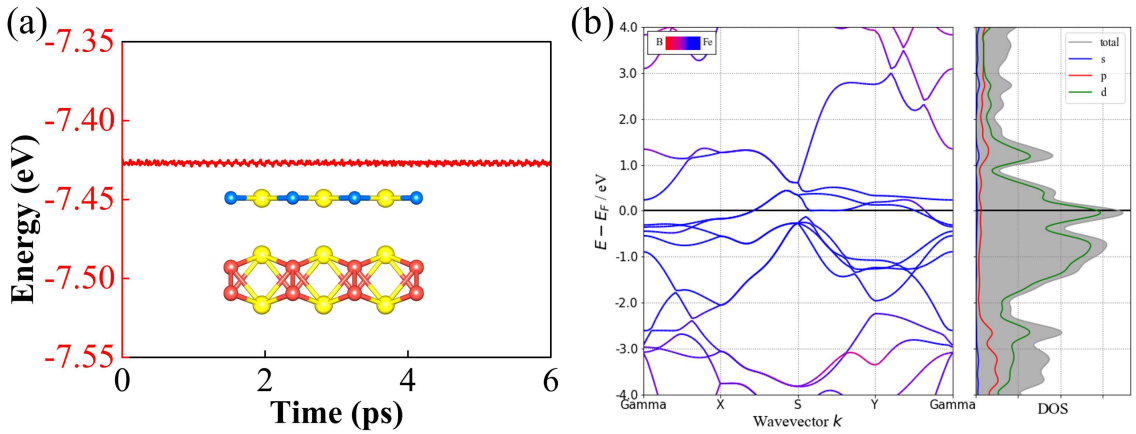

Figure S7: (a) The free energies per atom and the last snapshots of FeN/Fe_2B_2 heterojunction after being simulated by AIMD at 0K for 6 ps. (b) Calculated band structure of the 2D Fe_2B_2 monolayer in the magnetic ground state using HSE06 method. Only the spin-up channels are shown. The figure is plotted by pymatgen.[21]

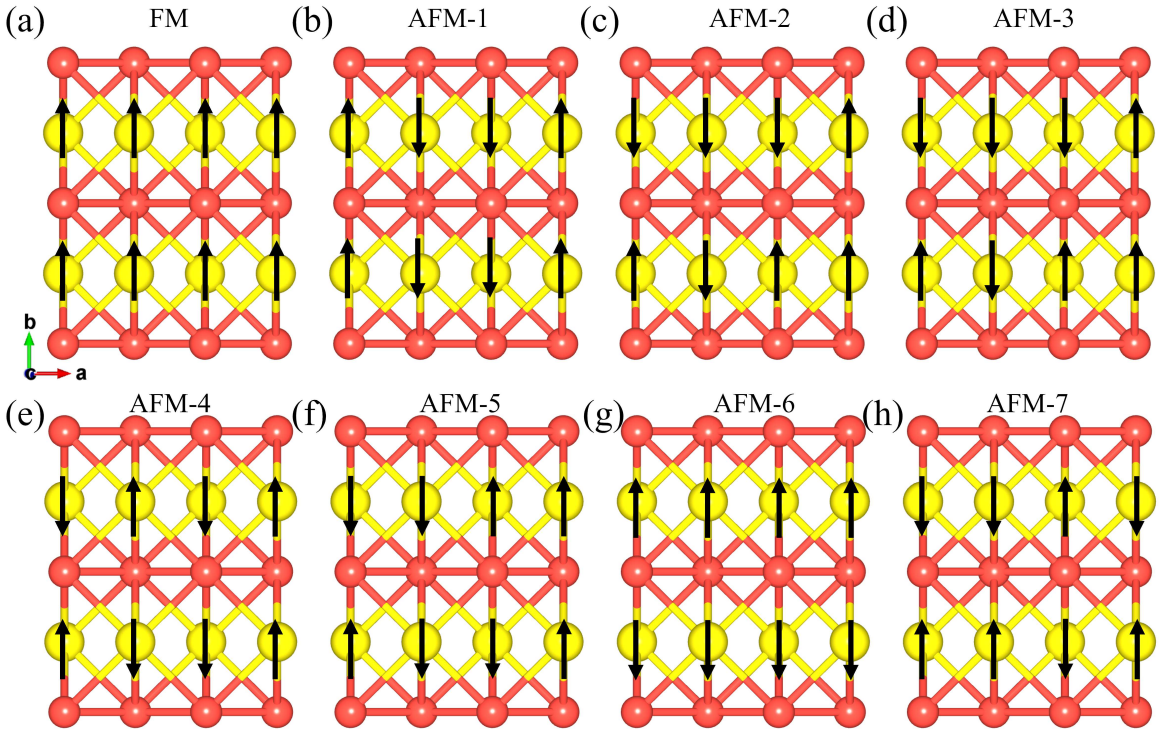

Figure S8: The ferromagnetic configuration (FM) of 2D Fe_2B_2. (b-h) The seven considered antiferromagnetic (AFM) configurations of 2D Fe_2B_2. Yellow balls represent the atoms of Fe. We demonstrated that the magnetic ground states of 2D Fe_2B_2 is AFM-6 configuration.

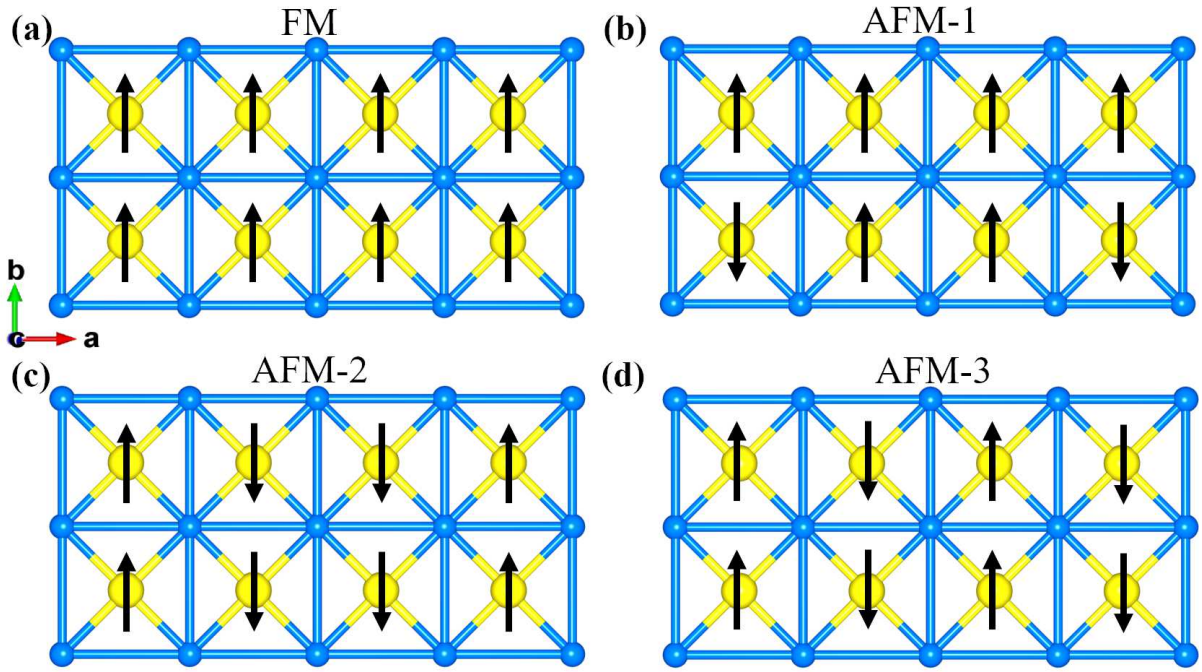

Figure S9: The ferromagnetic configuration (FM) of 2D FeN. (b-d) The three considered antiferromagnetic (AFM) configurations of 2D FeN. Yellow balls represent Fe atoms. The magnetic ground states is AFM-3.

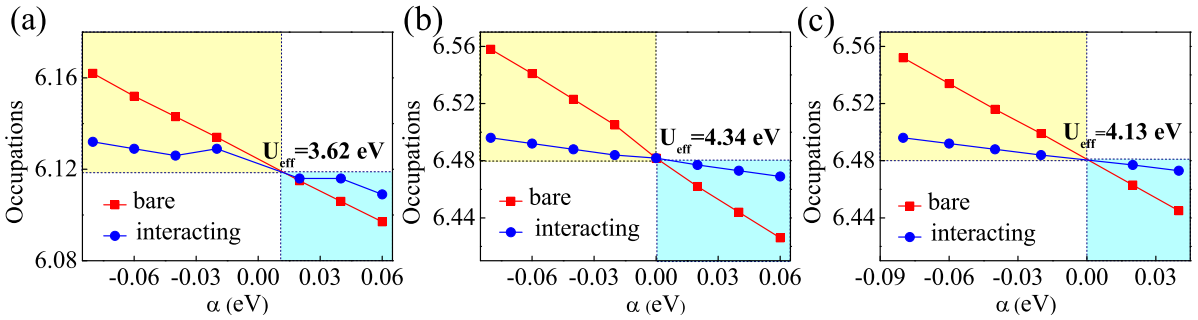

Figure S10: We computed the effective U_{eff} values of d for (a) FeN and (b-c) Fe_2B_2 of monolayers, respectively.

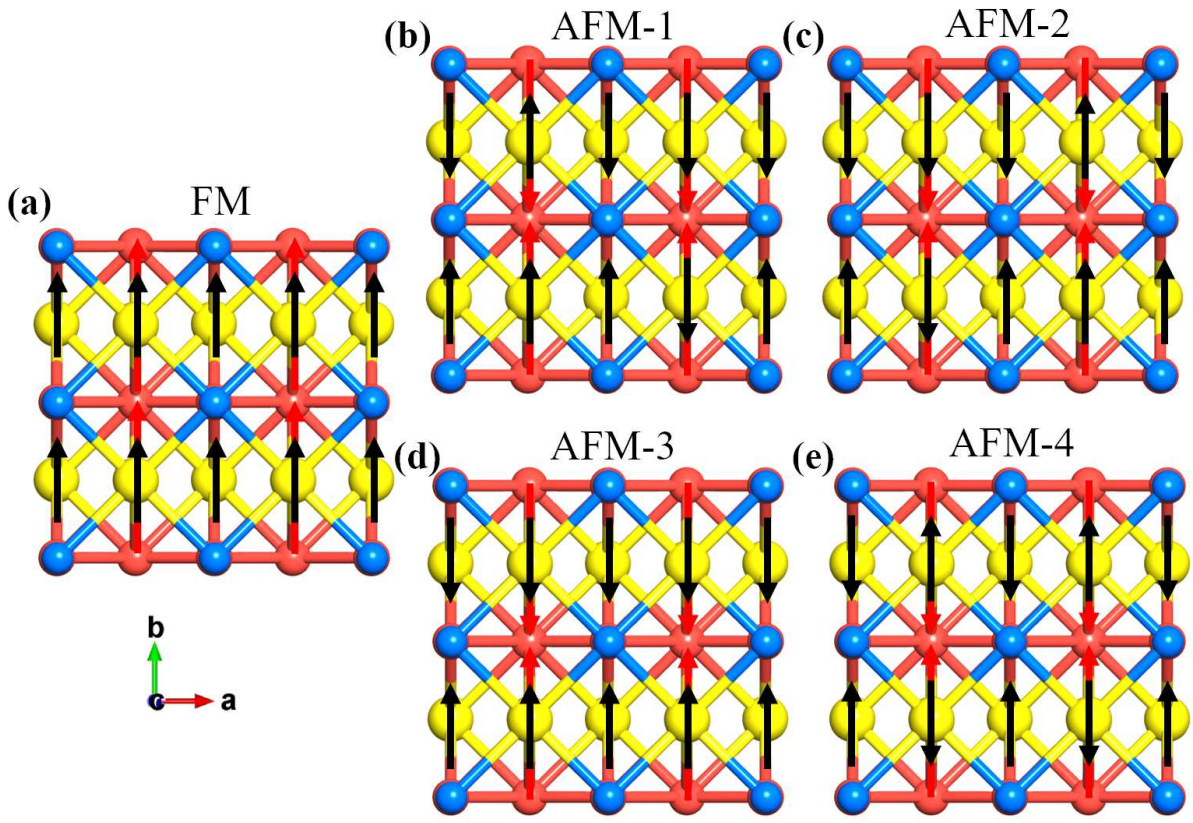

Figure S11: The ferromagnetic configuration (FM) of 2D FeN/Fe_2B_2 heterojunction. (b-e) The four considered antiferromagnetic (AFM) configurations of 2D FeN/Fe_2B_2 heterojunction. The red and black arrows indicate the bottom and the top layers Fe atoms, respectively. The magnetic ground state is AFM-3.

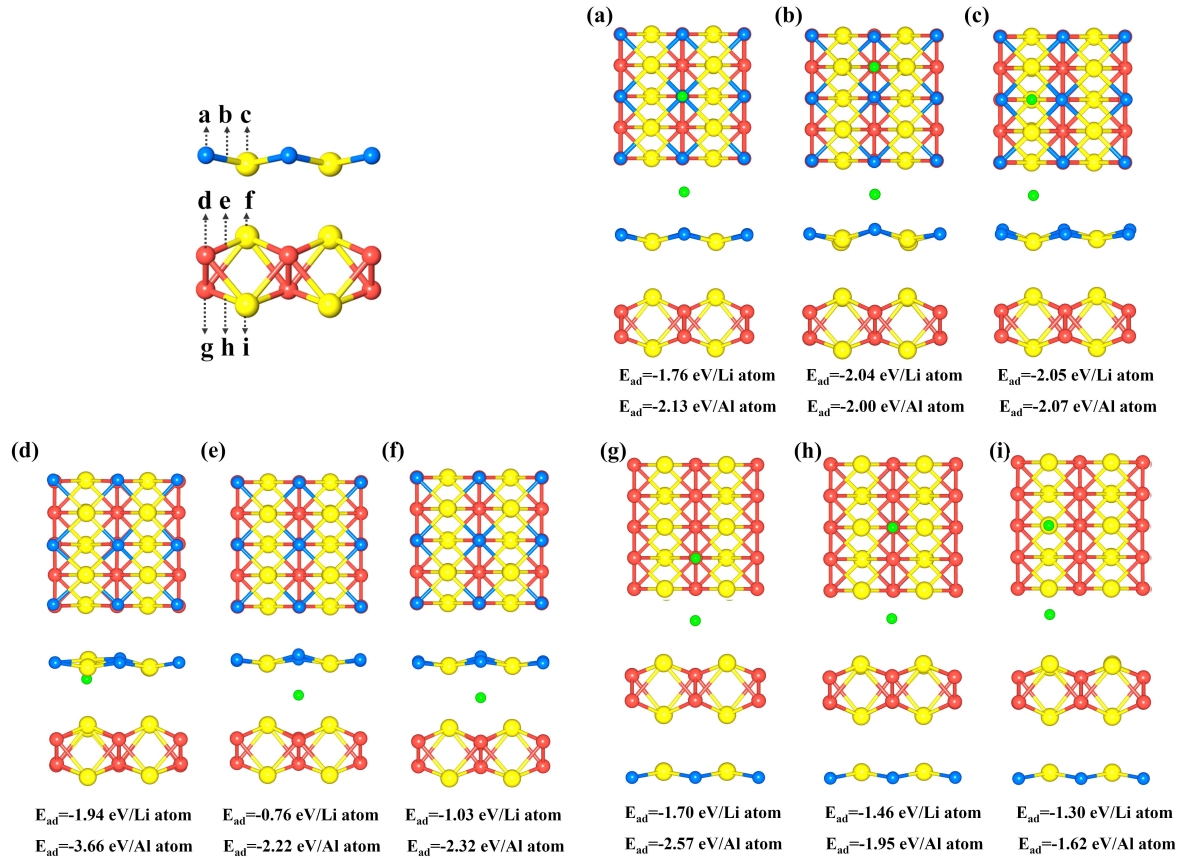

Figure S12: Optimized structure and the corresponding adsorption energy (E_{ad}) of single Li/Al atoms on four adsorption sites of the 2×2×1 FeN/Fe_2B_2 heterojunction, respectively.

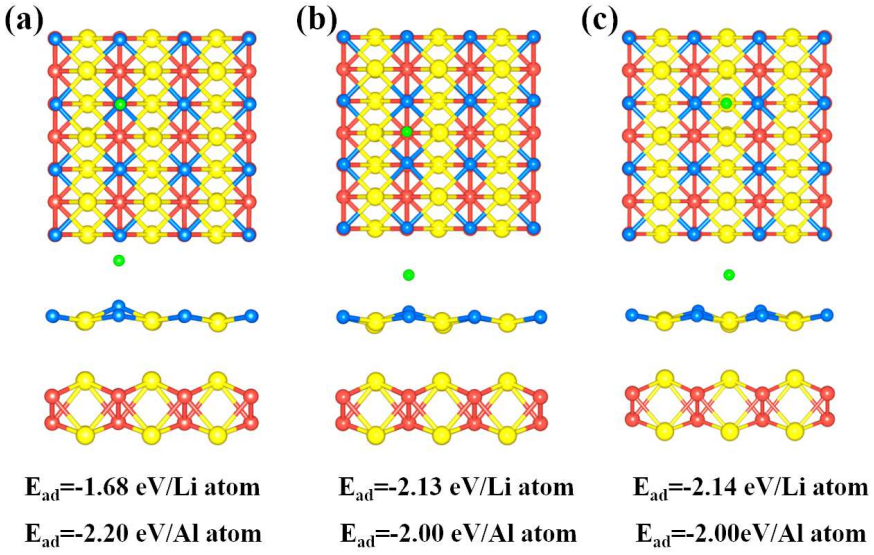

Figure S13: Optimized structure and the corresponding adsorption energy (E_{ad}) of single Li/Al atoms on four adsorption sites of the 3×3×1 FeN/Fe_2B_2 heterojunction, respectively.

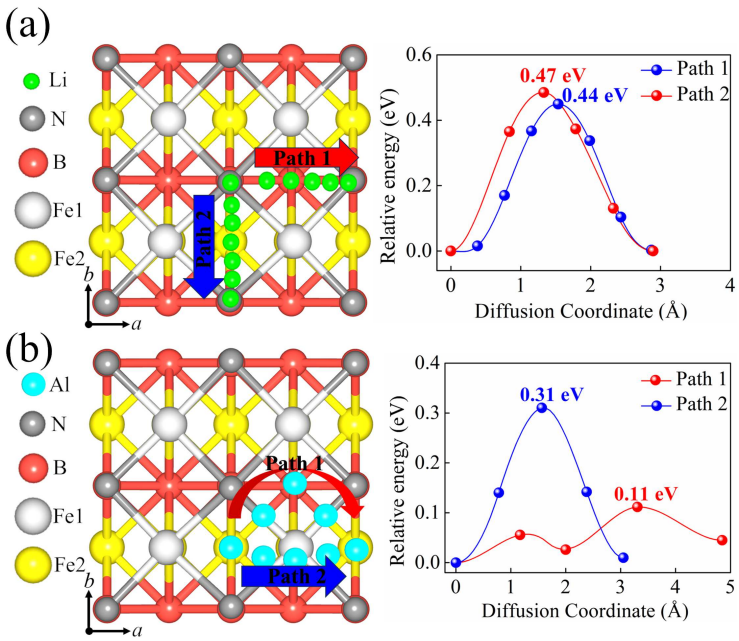

Figure S14: Energy profiles and atom diffusion barriers for (a) Li and (b) Al atoms at the interlayer of the FeN/Fe_2B_2 heterojunction. The top layer atoms are represented by gray balls.

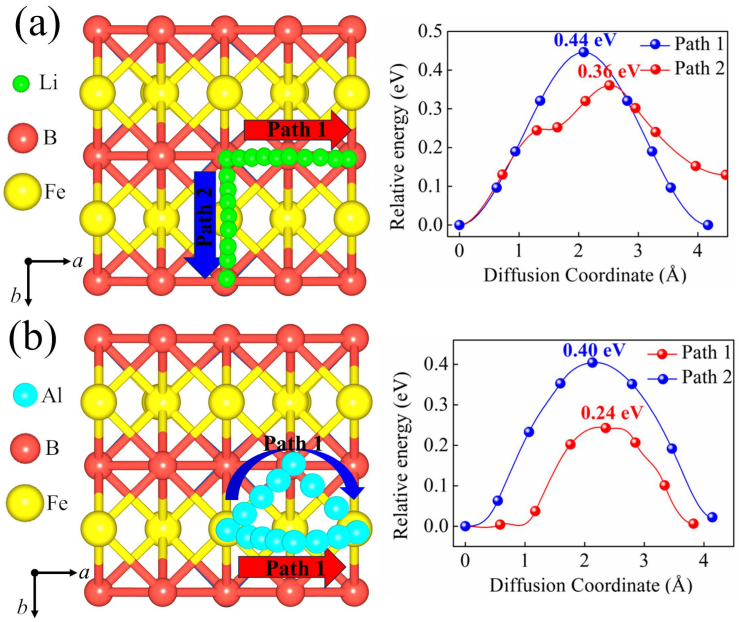

Figure S15: The energy profiles and atom diffusion barriers for (a) Li and (b) Al atom at the bottom layer of FeN/Fe_2B_2 heterojunction.

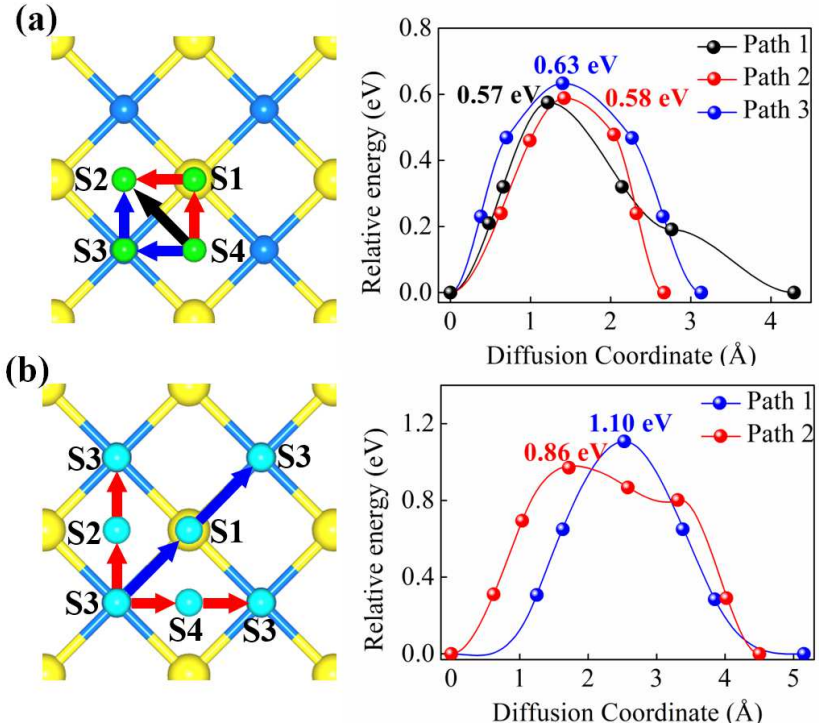

Figure S16: Possible (a) Li and (b) Al atom diffusion pathways and the energy barriers on the FeN monolayer. Paths 1, 2, and,3 are marked in black, red, and blue, respectively.

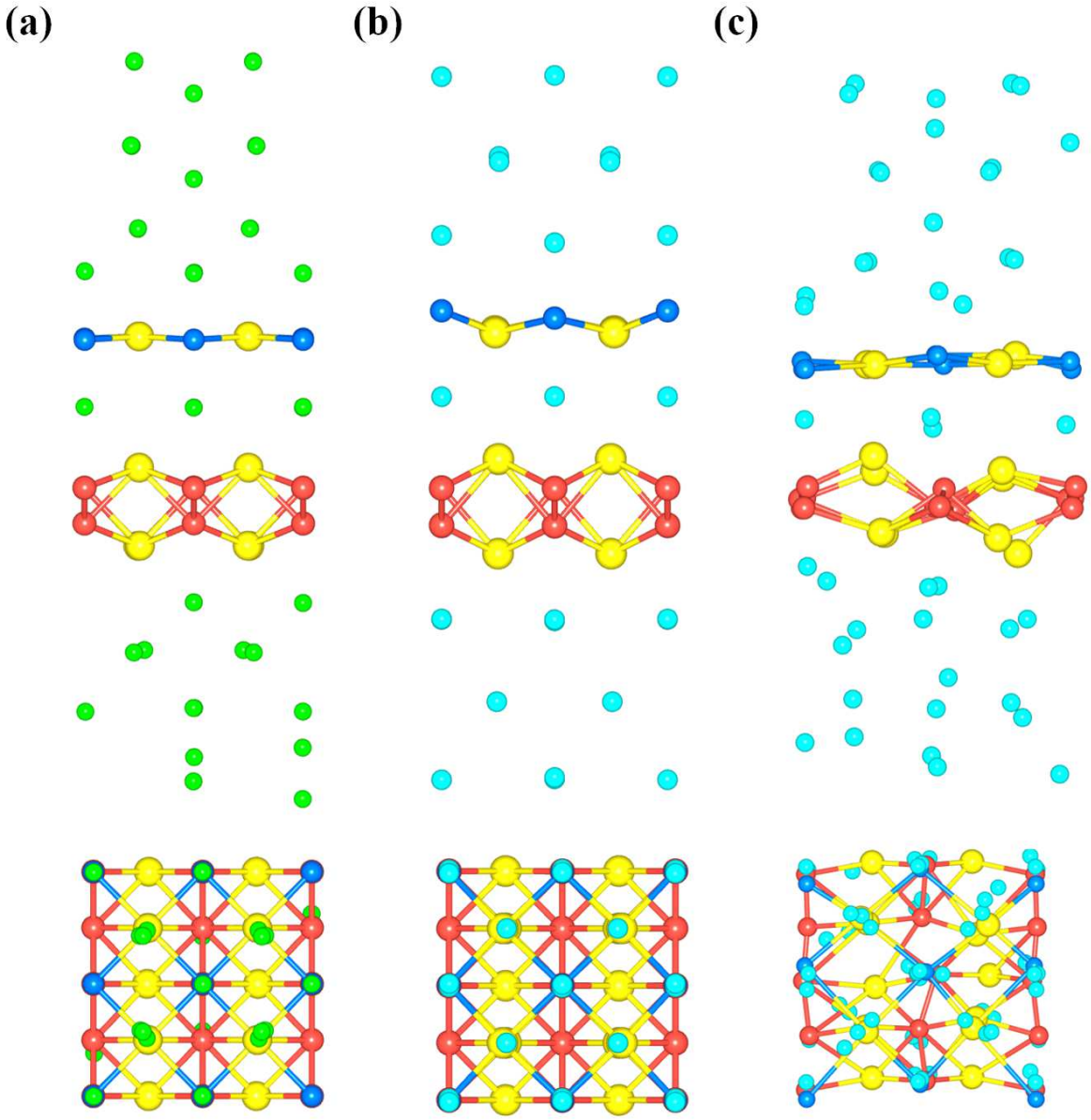

Figure S17: (a) Side and top views of the most stable structure with the maximum Li atom adsorbed on the FeN/Fe_2B_2 heterojunction. (b) Side and top views of the original structure with Al atoms. (c) Side and top views of the most stable structure with the maximum Al atoms adsorbed on the FeN/Fe_2B_2 heterojunction.

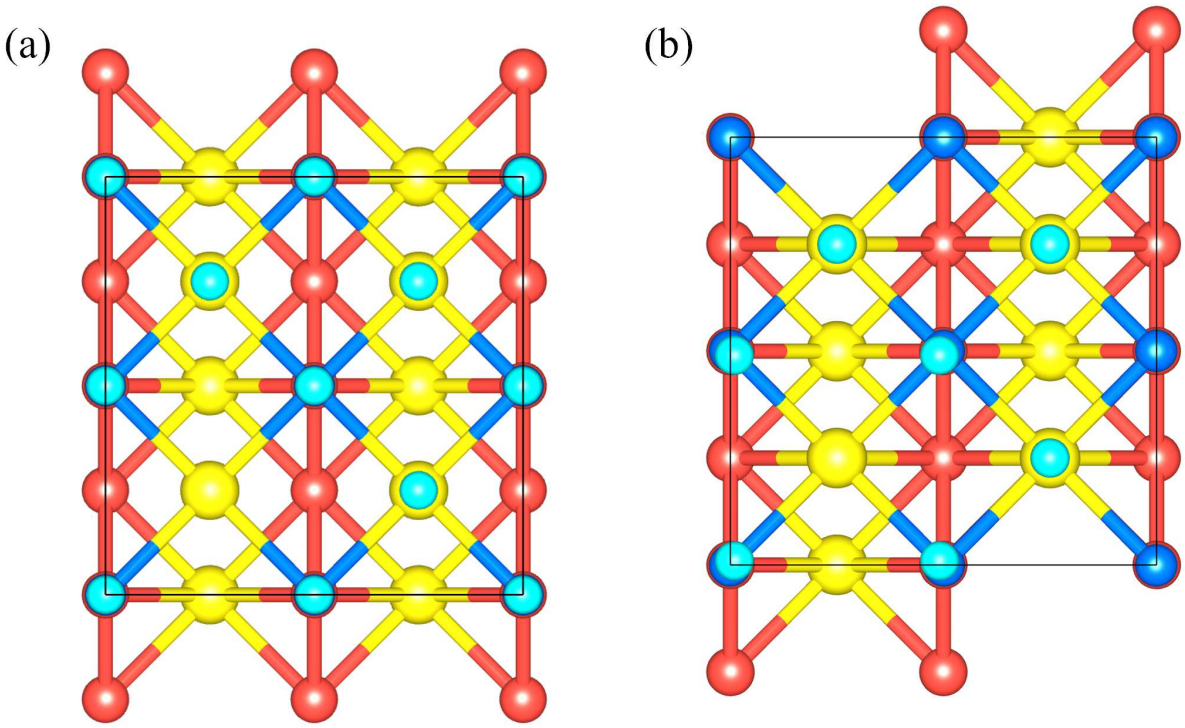

Figure S18: Top view of the FeN/Fe_2B_2 heterojunction with seven Al atom adsorbed sites: (a) the original structure, and (b) the stable structure after simulation in Monte Carlo method. The black lattice corresponds to the unit cell.

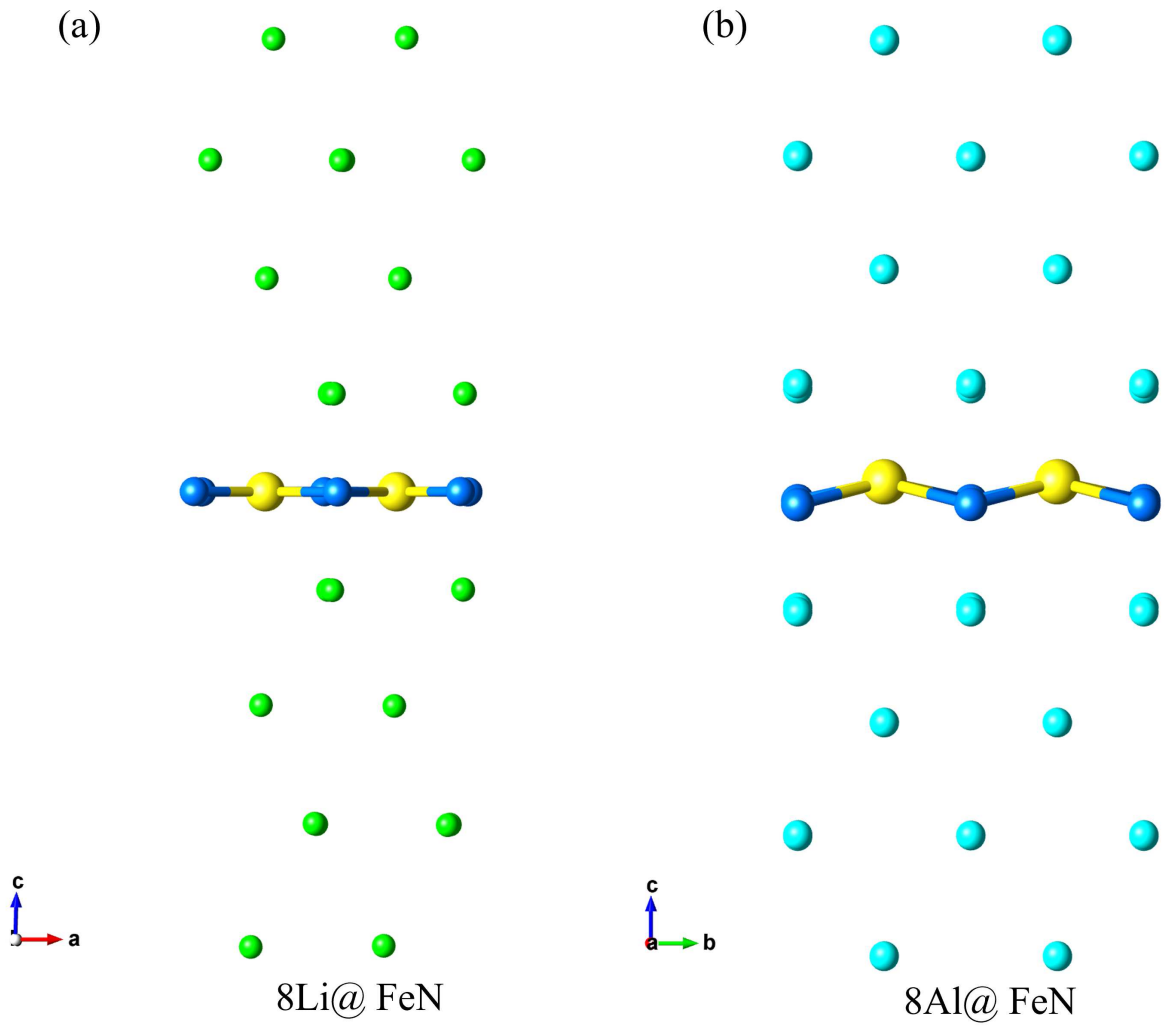

Figure S19: Side views of the most stable structure with the maximum concentration of (a) Li atoms and (b) Al atoms on the FeN monolayer.

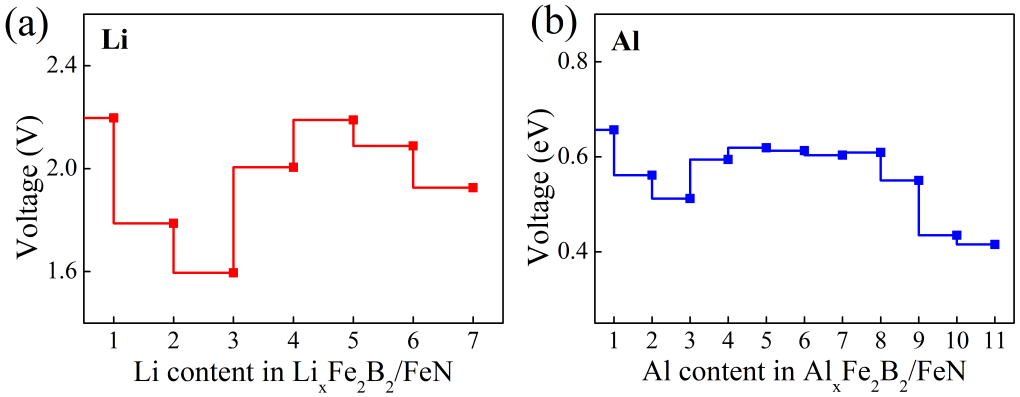

Figure S20: Calculated OCV of (a) Li and (b) Al as anode materials, as a function of specific capacity for the heterojunction.

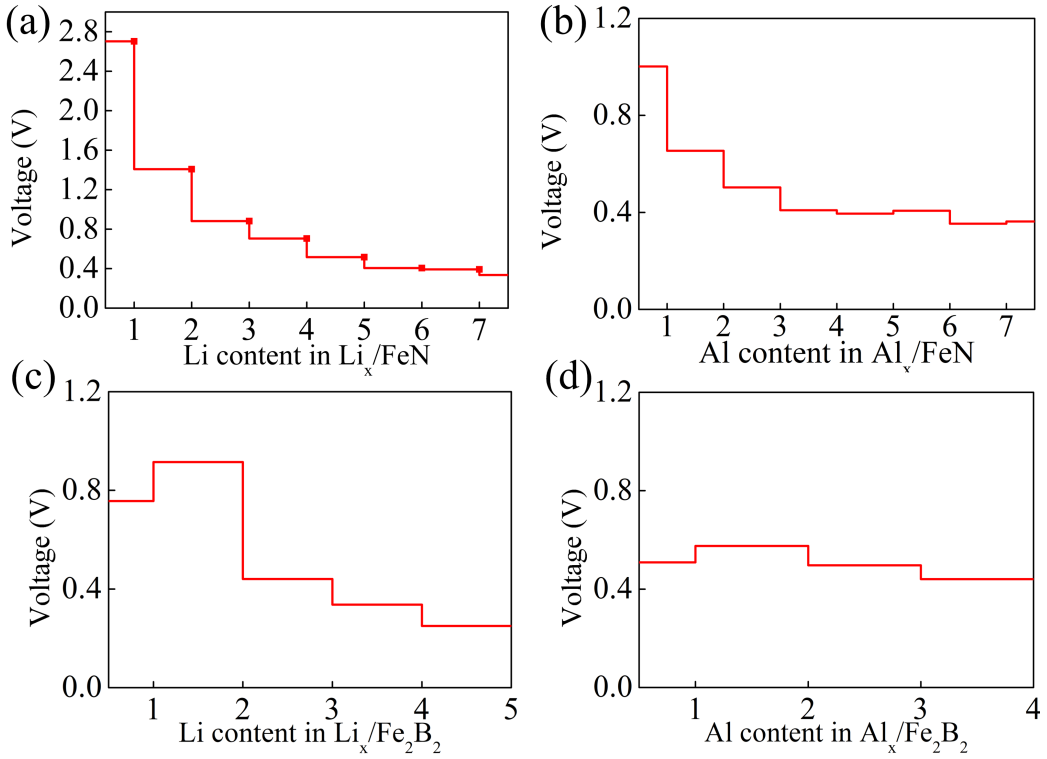

Figure S21: Calculated OCV of (a) Li and (b) Al as anode materials as a function of specific capacity for FeN monolayer. Calculated OCV of (c) Li and (d) Al as anode materials as a function of specific capacity for the Fe_2B_2 monolayer, respectively.

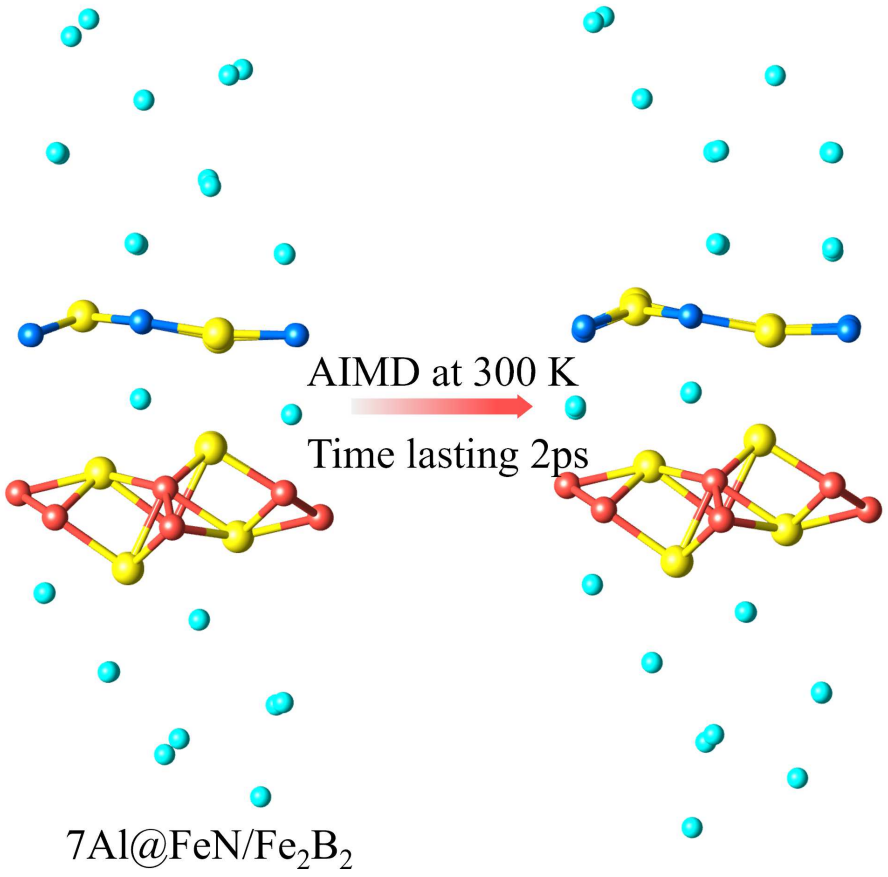

Figure S22: The calculated AIMD result for the structure of the 7Al@FeN/Fe_2B_2 heterojunction at 300 K, lasting 2 ps, shows that interlayer sliding is not observed.

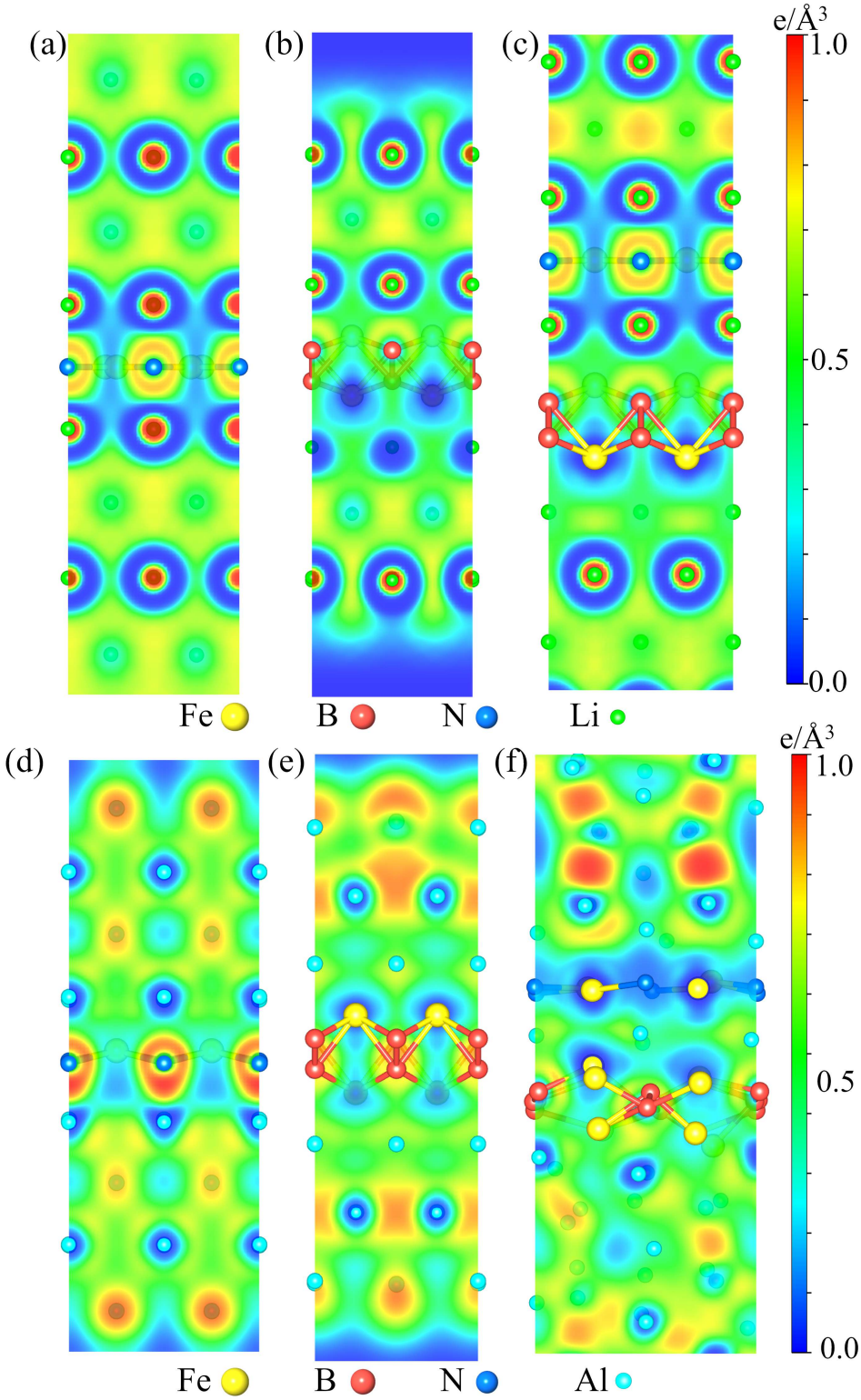

Figure S23: The electron localization function (ELF) maps sliced in the (100) direction for the (a) 8Li@FeN monolayer (b) 6Li@Fe_2B_2 monolayer, (c) 7Li@FeN/Fe_2B_2 heterojunction; (d) 8Al@FeN monolayer (e) 6Al@Fe_2B_2 monolayer (f) 10.75Al@FeN/Fe_2B_2 heterojunction.

References

(1) Ke, C.; Fan, D.; Chen, C.; Li, X.; Jianga, M.; Hu, X. Two-Dimensional Tetragonal Transition-Metal Carbide Anodes for Non-Lithium-ion Batteries. *Phys. Chem. Chem. Phys.,* **2020.** 22. 13680-13688.

(2) Liu, H.; Wang, H.; Jing, Z.; Wu, K.; Cheng, Y.; Xiao, B. Bare Mo-Based Ordered Double-Transition Metal MXenes as High Performance Anode Materials for Aluminum-Ion Batteries. *J. Phys. Chem. C* **2020.** 124, 25769-25774.

(3) Ding, Y.; Deng, Q.; You, C.; Xu, Y.; Lia, J.; Xiao, B. Assessing Electrochemical Properties and Diffusion Dynamics of Metal Ions (Na, K, Ca, Mg, Al and Zn) on a C_2N Monolayer as an Anode Material for Non-Lithium Ion Batteries. *Phys. Chem. Chem. Phys.,* **2020.** 22. 21208-21221.

(4) Bai, T.; Liu, H.; Chen, B.; Qiu, Y.; Dong, H.; Wu, K.; Cheng, Y.; Xiao, B. Assessing $(Mo_{2/3}Sc_{1/3})_2C$ and $(Mo_{2/3}Sc_{1/3})_2CT_2$(T=-O, -OH, and -F) i-MXenes as High-Performance Electrode Materials for Lithium and Non-Lithium Ion Batteries. *J. Phys. Chem. C* **2022**. 126. 10273-10286.

(5) Lee, S.; Jung, S. C.; Han, Y. Fe_2CS_2 MXene: A Promising Electrode for Al-ion Batteries. *Nanoscale*. **2020**. 12. 5324.

(6) Vakili-Nezhaada, G. R.; Gujarathia, A. M.; Rawahi, N. A.; Mohammadic, M. Performance of WS_2 Monolayers as a New Family of Anode Materials for Metal-Ion (Mg, Al and Ca) Batteries. *Mater. Chem. Phys.* **2016.** 183. 392-397.

(7) Deng, X.; Chen, X.; Huang, Y.; Xiao, B.; Du, H. Two-Dimensional GeP_3 as a High Capacity Anode Material for Non Lithium-Ion Batteries. *J. Phys. Chem. C* **2019**. 123. 4721-4728.

(8) Rao, S.; Zhang, L.; Meng, Z.; Zhang, X.; Wang, Y.; Qiao, G.; Shen, X.; Xia, H.; Liu, J.; Lu, R. Ultrahigh Energy Storage and Ultrafast Ion Diffusion in Borophene-Based Anodes for Rechargeable Metal Ion Batteries. *J. Mater. Chem. A,* **2017**. 5. 2328.

(9) Li, P.; Li, Z.; Yang, J.; Rational Design of Two-dimensional Anode Materials: B_2S as a Strained Graphene. *J. Phys. Chem. Lett.* **2018**. 9. 4852-4856.

(10) Wang, S.; Miao, N.; Su, K.; Blatov, V. A.; Wang, J. Discovery of Intrinsic Two-Dimensional Antiferromagnets From Transition-Metal Borides. *Nanoscale*. **2021**. 13. 8254.

(11) Andrew, R. C.; Mapasha, R. E.; Ukpong, A. M.; Chetty, N. *Phys. Rev. B*. **2012.** 85. 125428.

(12) Mannix, A. J.; Zhou, X F.; Kiraly, B.; Wood, J. D.; Alducin, D.; et al. Synthesis of Borophenes: Anisotropic, Two-Dimensional Boron Polymorphs. *Science*. **2015**. 350. 1513-1516.

(13) Wu, X.; Pei, Y.; Zeng, X. C. B_2C graphene, nanotubes, and nanoribbons. *Nano Lett.* **2009**. 9. 1577-1582.

(14) Zhang, M.; Tang, C.; Wang, C.; Cheng W.; Fu, L. The First-Principles Study on The Performance of The Graphene/WS_2 Heterostructure as an Anode Material of Li-Ion Battery. *J. Alloys Compd.* **2021**. 855. 157432.

(15) Fan, D.; Lu, S.; Guo, Y.; Hu, X. Two-Dimensional Stoichiometric Boron Carbides with Unexpected Chemical Bonding and Promising Electronic Properties. *J. Mater. Chem. C*. **2018**. 6. 1651-1658.

(16) Ye, X. J.; Li, T. K.; He, J. J.; Wang, X. F.; Liu, C. S. Magnesene: A Theoretical Prediction of a Metallic, Fast, High-Capacity, and Reversible Anode Material for Sodium-Ion Batteries. *Nanoscale*. **2022**. 14. 6118-6125.

(17) Zhu, C.; Lin, S.; Zhang, M.; Li, Q.; Su, Z.; Chen, Z. Ultrahigh Capacity 2D Anode Materials for Lithium/Sodium-Ion Batteries: an Entirely Planar B_7P_2 Monolayer with Suitable Pore Size and Distribution. *J. Mater. Chem. A*. **2020**. 8. 10301.

(18) Muraleedharan, M. G.; Kent, P. R. C. Novel Boron Nitride MXenes as Promising Energy Storage Materials. *Nanoscale*. **2022**. 14. 9086-9096.

(19) Guo, G. C.; Wang, R. Z.; Ming, B. M.; Wang, C.; Luo, S. W.; Lai, C.; Zhang, M. Trap Effects on Vacancy Defect of C_3N as Anode Material in Li-Ion Battery. *Appl. Surf. Sci.* **2019**. 475. 102-108.

(20) Guo, G.; Tang, X.; You, M.; Luo, S.; Huang, Z.; Wei, X.; Wang, R.; Zhang, J. Defect-Independent Migration of Li on C_3B for Li-Ion Battery Anode Material. *Solid State Ion.* **2022**. 380. 115939.

(21) Ong, S. P.; Richards, W. D.; Jain, A.; Hautier, G.; Kocher, M.; Cholia, S.; Gunter,D.; Chevrier, V. L.; Persson, K. A.; Ceder, G. PyMatgen: A Robust.Open-SourcePython Library for Materials Analysis.*Comp. Mater. Sci.* **2013.** 68. 314-319.